CONF-790528--1

LA-UR 79-1043

MASTER

TITLE: NUCLEAR CHARGE RADII OF THE $1F_{7/2}$ SHELL NUCLEI FROM MUONIC ATOMS

AUTHOR(S): H. D. Wohlfahrt

SUBMITTED TO: Invited talk at the International Discussion Meeting about "what do we know about radial shape of Nuclei in the Ca region?" in Karlsruhe, Germany, May 2-4, 1979; talk will be published in the Conference Proceedings.

University of California
LOS ALAMOS SCIENTIFIC LABORATORY
Post Office Box 1663 Los Alamos, New Mexico 87545
An Affirmative Action/Equal Opportunity Employer

Form No. 836 R3
St. No. 2629
12/78

UNITED STATES
DEPARTMENT OF ENERGY
CONTRACT W-7405-ENG. 36

NUCLEAR CHARGE RADII OF THE $1F_{7/2}$ SHELL NUCLEI FROM MUONIC ATOMS

H. D. Wohlfahrt
Los Alamos Scientific Laboratory
Los Alamos, New Mexico 87545

I. Introduction

The experimental accuracy obtained in recent measurements of charge radii shows clearly that the usual empirical mass-radius formulae [e.g. 1,2] are only approximate. The variations of actual charge radii are strongly modified by nuclear shell structure and deformation effects [3,4]. The deviations of the measured charge radii from the mass-radius formulae seem to follow regular trends as indicated by Fig. 1.

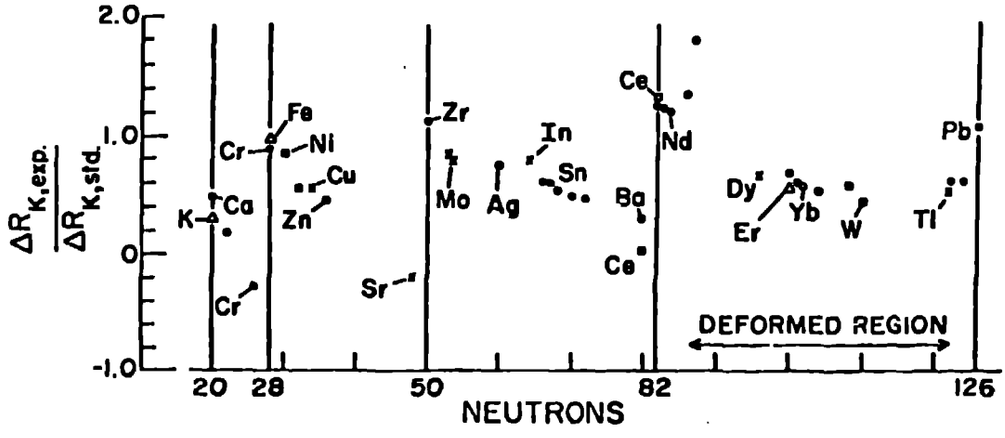

Fig. 1. $\Delta N = 2$ isotope shifts from muonic x-ray measurements prior to 1974.

The figure represents a compilation of muonic isotope shift data [5] taken prior to 1974. It shows $\Delta N = 2$ charge radii differences for even nuclei

as a function of the neutron number. To emphasize the departure of the data from the mass-radius formulae, the experimental shift values have been divided by "standard" shift values, calculated with a mass-radius formula. The data available in 1974 [5] indicate that the isotope shifts are largest at the beginning of a neutron shell and become quite small just before the major shell closures N = 28, 50, 82 and 126. This trend is especially pronounced in the $1f_{7/2}$ shell ($20 < N \leq 28$), where large negative isotope shifts occur at the end of the shell.

To investigate these trends in detail, muonic x-ray studies of medium-weight nuclei have been performed in recent years by the Los Alamos muonic x-ray group, using the high intensity muon beam available at the LAMPF 800 MeV proton accelerator. Fig. 2 shows the $1f_{7/2}$ shell nuclei investigated [3,6,7]. These studies, which together include all stable $1f_{7/2}$ neutron shell nuclei, provide information about the proton core polarization due to the successive addition of neutrons for the proton cores Z = 20(Ca), 22(Ti), 24(Cr), 26(Fe) and 28(Ni). In addition, these studies, which represent the first systematic investigations of isotone shifts, provide the opportunity to compare the core polarization caused by protons with core polarization caused by neutrons in the same ($1f_{7/2}$) shell.

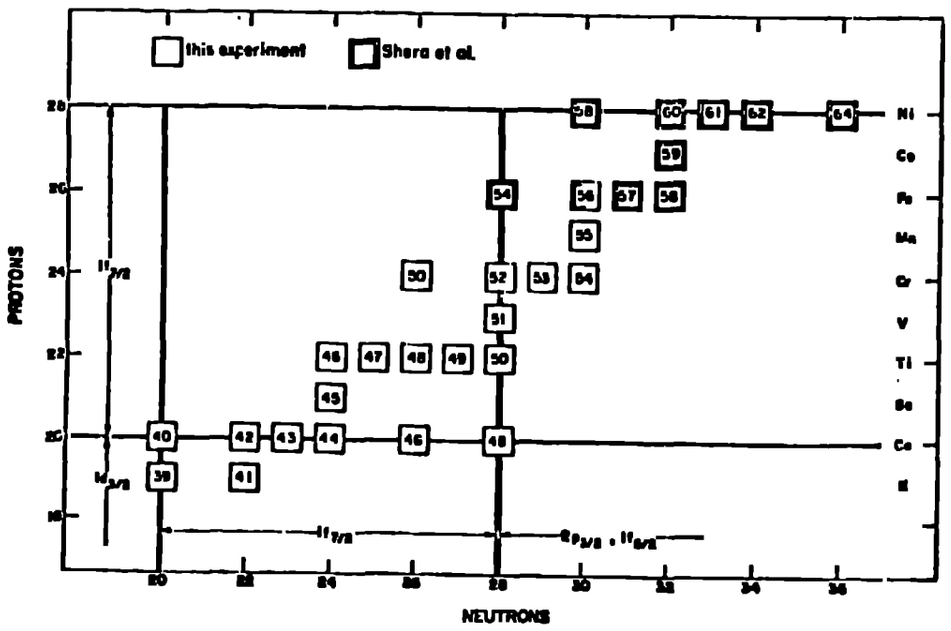

Fig. 2 Investigated nuclei and associated shell model configuration.

II. Nuclear Charge Distribution Parameters from Muonic Atoms

Fig. 3 illustrates 2p and 1s muonic energy levels for ^{40}Ca. The muon which has lost nearly all of its kinetic energy is captured in a high orbital and forms a muonic atom. The excited muonic atom decays mainly via electric dipole transitions and may reach states, where the overlap between the muon wave function and the nuclear charge distribution causes a measureable energy shift ΔE^{FS} of the binding energy from the binding energy calculated for a point nucleus E_B^{PN}. In the $1f_{7/2}$ shell nuclei, only in the 1s state is the

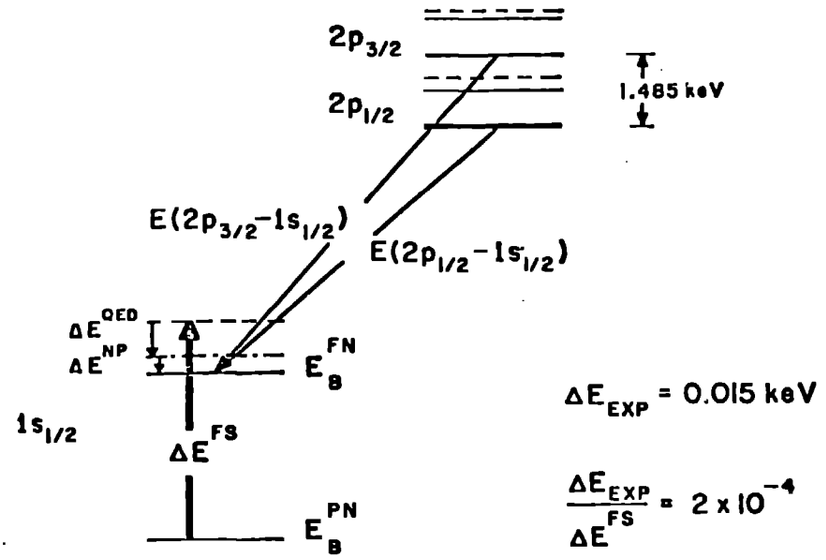

Fig. 3. Muonic (2p-1s) transitions. For exact scaling (^{40}Ca) see Table I.

finite size effect ΔE^{FS} large compared with the experimental error for determining muonic binding energies (15 eV). Table 1 lists ΔE^{FS} and E_B^{PN} for the 1s and 2p states. Note that the finite size effect in the 1s state (69.117 keV) is very large compared with the experimental error (15 eV), so the finite

State	E_B^{PN}/keV	ΔE^{FS}/keV	ΔE^{QED}/keV	ΔE^{NP}/keV
$1s_{1/2}$	1128.157	-69.117	6.810(20)	0.170(50)
$2p_{1/2}$	282.418	-0.087	0.929	0.001
$2p_{3/2}$	280.904	-0.033	0.904	0.001

Table I. Point nucleus binding energy E_B^{PN}, finite size effect ΔE^{FS}, quantum electrodynamical corrections ΔE^{QED} and nuclear plozarization correction ΔE^{NP} for the muonic ^{40}Ca atom in(keV).

size effect can be determined with a relative accuracy of about 2×10^{-4}. In the 2p states, which are separated by about 1.5 keV due to the fine-structure splitting, the finite size effect is about 3 orders of magnitude smaller than in the 1s state and ΔE_{2p}^{FS} is comparable to the experimental error. Therefore the experimentally observed 2p-1s transitions contain only information about the finite size effect in the 1s state. To deduce the finite size effect from the measured transition energies, theoretical corrections have to be included. The quantum electrodynamical corrections ΔE^{QED} (mainly vacuum polarization and lamb-shift) of about 7 keV in the 1s state of ^{40}Ca are known with an accuracy of about 20 eV [8]. Nuclear polarization corrections ΔE^{NP}, which consider the polarizibility of the nucleus in the presence of the muon, are known much less accurately. An uncertainty of 30% is commonly attributed to these corrections, which results in an uncertainty of about 50 eV (see Table I). The uncertainty of the derived nuclear charge distribution parameters is therefore mainly determined by the uncertainty of the theoretical corrections, which is about 5 times larger than the experimental errors in the case of the $1f_{7/2}$ shell nuclei. However in the differences of the nuclear charge distribution parameters for neighboring isotopes, these uncertainties cancel to a high degree.

First order perturbation theory can tell us what information we may obtain from a muonic atom. In this context the finite size energy shift in a muonic transition is given by:

$$\Delta E_{i,f}^{FS} = \int_0^\infty \rho(r)\left[V_\mu^i(r) - V_\mu^f(r)\right] 4\pi r^2 dr - Z\left[V_\mu^i(0) - V_\mu^f(0)\right] \quad , \tag{1}$$

where V_μ^i and V_μ^f are the potentials produced by the bound muon in the initial and final states. As Barrett [9] has shown, these differences in the potentials can be approximated by an analytical expression of the form $A + Br^k e^{-\alpha r}$ In principal all 4 parameters A, B, k and α depend on $\rho(r)$, Z, n and l. The measured quantity in a muonic atom experiment can therefore be written as

$$\langle r^k e^{-\alpha r} \rangle = \frac{4\pi}{Z} \int_0^\infty \rho(r, r^k e^{-\alpha r} r^2 dr \quad , \tag{2}$$

the Barrett moment of the charge distribution.

In the actual analysis of the muonic data we adjust the parameters of a Fermi charge distribution

$$\rho_F(r) = \rho_0 \, (1 + \exp(r - c)/a)^{-1} \tag{3}$$

to the measured transition energies by solving the Direc equation including all higher order corrections. In the case of the $1f_{7/2}$ shell nuclei only the half density radius c was adusted; the parameter a was fixed at 0.55 fm, which corresponds to a surface thickness parameter t = 2.42 fm. From the muon wave function, determined by solving the Direc equation, the potential produced by the bound muon $V_\mu(r)$ can be deduced and the potential parameters A, B, k and α can be adjusted to fit the difference $V_\mu^i - V_\mu^f$. For the $1f_{7/2}$ shell nuclei ($20 \leq Z \leq 28$) we obtain a range of values of $2.114 \leq k \leq 2.121$ and $0.064 fm^{-1} \leq \alpha \leq 0.074\ fm^{-1}$ for the 2p-1s transitions. With these values of k and α, we can calculate the appropriate Barrett moments using equation 2.

These Barrett moments deduced using Fermi charge distributions are model-independent (at least to the level of accuracy set by the experimental errors). That is, a realistic charge distribution (for example, from electron scattering) with the same Barrett moment $\langle r^k e^{-\alpha r} \rangle$ as the adjusted Fermi charge distribution gives a transition energy equal to the observed transition energy within the experimental error. From the Barrett moments one can obtain model-independent equivalent radii R_k defined by:

$$3R_k^{-3} \int_0^{R_k} r^k e^{-\alpha r} r^2 dr = \frac{4\pi}{Z} \int_0^{\infty} \rho_F(r) r^k e^{-\alpha r} r^2 dr \tag{4}$$

For the comparison of the results from muonic x-ray experiments with those of other experiments and with theory, it is very convenient to have rms-radii $\langle r^2 \rangle^{1/2}$ instead of equivalent radii R_k. From muonic data alone rms-radii cannot be determined model-independently, since the radial shape of the charge distribution is not known. This fact can be easily shown by

changing the surface thickness parameter of the Fermi charge distribution by 10% and readjusting the half density radius to maintain the same transition energy. The resulting R_k changes by only 0.1×10^{-3}fm, whereas, the rms-radius changes by 5×10^{-3}fm. This change is large compared with the experimental error of 0.4×10^{-3}fm.

To obtain model-independent rms-radii we performed a combined analysis of our muonic data and electron scattering data from Stanford [10] (Ca and Ti) and Mainz [11] (Fe and Ni). The analysis used was based on the Fourier-Bessel expansion [12] of the charge distribution. With the radial shape of the charge distribution obtained from electron scattering, an extrapolation from the precise muonic Barrett moments to the rms-radii can be performed in this combined analysis without substantial loss of accuracy. In the following, I will present the results of such combined analyses.

III. Experimental Arrangement and Measurements

Before I present the experimental results, let me briefly discuss the experimental arrangement and the analysis of the measured spectra. At the time of the $1f_{7/2}$ shell experiment, LAMPF was running at a proton beam current of 150μA; the muon rates used in our measurements were about 10^5/sec. Fig. 4 shows our experimental target arrangement. The scintillators S_1, S_2 and S_3^i

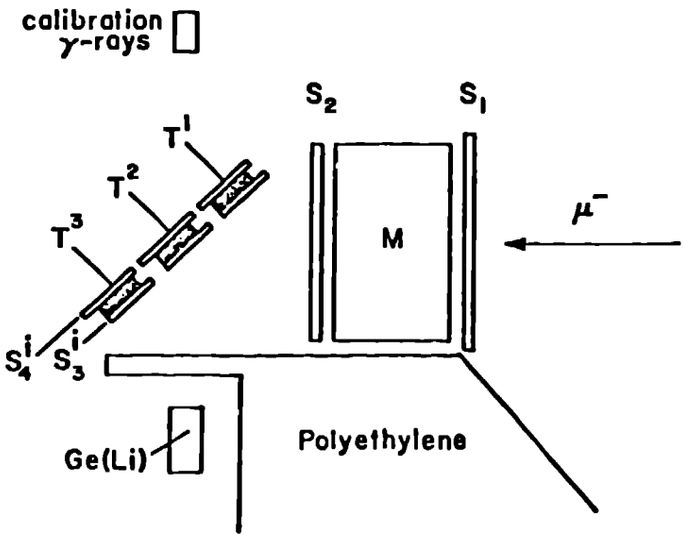

Fig. 4. Arrangement of scintillation counter telescope (S_i), muon moderator (M), targets (T^i), and Ge(Li) detector.

in anti-coincidence to S_4^i signal a stopped muon in one of the three simultaneously measured targets T^i. An x-ray event in the Ge(Li) in coincidence with $S_1\ S_2\ S_3^i\ \bar{S}_4^i$ is identified as a muonic x-ray. Simultaneously with the x-rays, we measure γ-rays from various calibration sources, using a beam gating technique to insure that the calibration spectra are stored at an average rate which is proportional to the intensity of the muonic x-rays. A sophisticated interface in connection with an on-line computer insures that the different events are stored in their respective spectra, and that ambiguous events are discarded. Eleven calibration lines, known with an individual accuracy of 5 eV, covered the energy region of interest (650-1600 keV) for the experiment. These lines provided both the energy calibration for the muonic x-ray lines and spectral line shape parameters used in the fitting of the muonic lines.

Fig. 5 shows the muonic 2p-1s x-ray doublets for Ti and Cr isotopes. The isotope shifts of the x-ray energies have opposite signs for ^{50}Ti-^{48}Ti and ^{54}Cr-^{52}Cr. The curves are "best fits" to the measured spectra considering the known isotopic impurities.

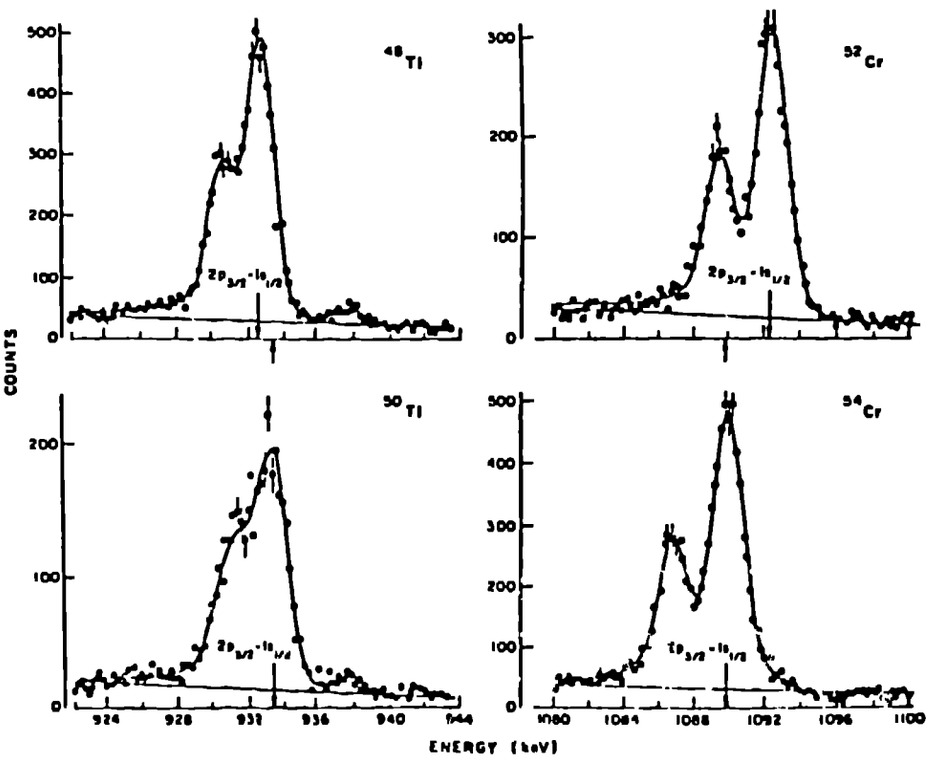

Fig. 5. Muonic x-ray spectra for Ti and Cr isotopes.

IV. Experimental Results and Interpretation

A. Discussion of the observed systematics

A graphical summary of our results for the $1f_{7/2}$ shell nuclei is shown in Fig. 6. The display shows rms-charge radii obtained from the combined analysis of the muonic data [3,6,7] and elastic electron scattering data [10,11], as a function of the neutron and proton number respectively. The Ca isotopes, which cover the whole $1f_{7/2}$ neutron shell, show increasing radii in the first half of the shell from ^{40}Ca to ^{44}Ca and decreasing radii in the second half of the shell from ^{44}Ca to ^{48}Ca. The increase in the first half of

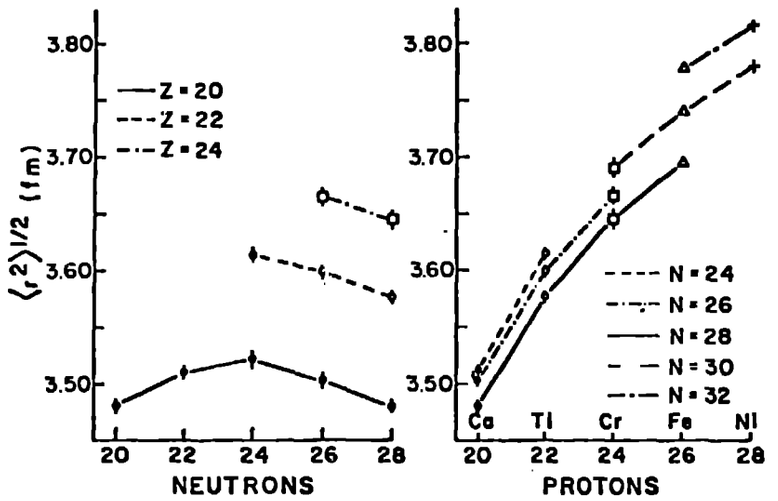

Fig. 6. Rms-charge radii for the $1f_{7/2}$ shell nuclei from a combined analysis of the muonic data and (e,e) data.

the shell is totally compensated by the decrease in the second half of the shell resulting in a net rms-charge radius change of zero for ^{40}Ca-^{48}Ca (within the experimental error of about 1×10^{-3}fm). The Ti and Cr isotopes, which are situated in the second half of the shell, show decreasing radii with increasing neutron number like the heavier Ca's. In the right part of Fig. 6 isotone shifts for the different isotone sequences involving the neutron numbers $24 \leq N \leq 32$ are displayed. Two features are apparent: 1. The curves for the various isotones are parallel. 2. A saturation effect exists; the magnitude of the increase in the rms-radii becomes smaller with increasing proton number.

To emphasize the observed effects, Fig. 7 displays the changes in the rms-radii between even neighboring isotones and isotopes. Both the isotone

and isotope $\delta\langle r^2\rangle^{1/2}$ shifts show an almost linear decrease in the radii differences with increasing proton and neutron number, respectively. Both the isotone and isotope shifts are independent of the neutron or proton configuration of the particular nuclei. That is, the Z = 20 proton core of the Ca isotopes shows the same polarizibility as the Z = 22 and Z = 24 proton cores of the Ti and Cr isotopes. Similar results had been obtained earlier from our studies of nuclei in the Ni region [3]. Thus, the Z = 28 proton core of the Ni isotopes shows the same polarizibility as the Z = 26 and Z = 30 proton cores of the Fe and Zn isotopes. These experimental results suggest that the added neutrons interact with the whole proton core rather then with the valence protons. The dashed lines in the figures above indicate that the slopes of the isotone and isotope shifts are almost the same. Both sets of data show a strong shell structure effect when crossing the shell closure at Z or N equal 28.

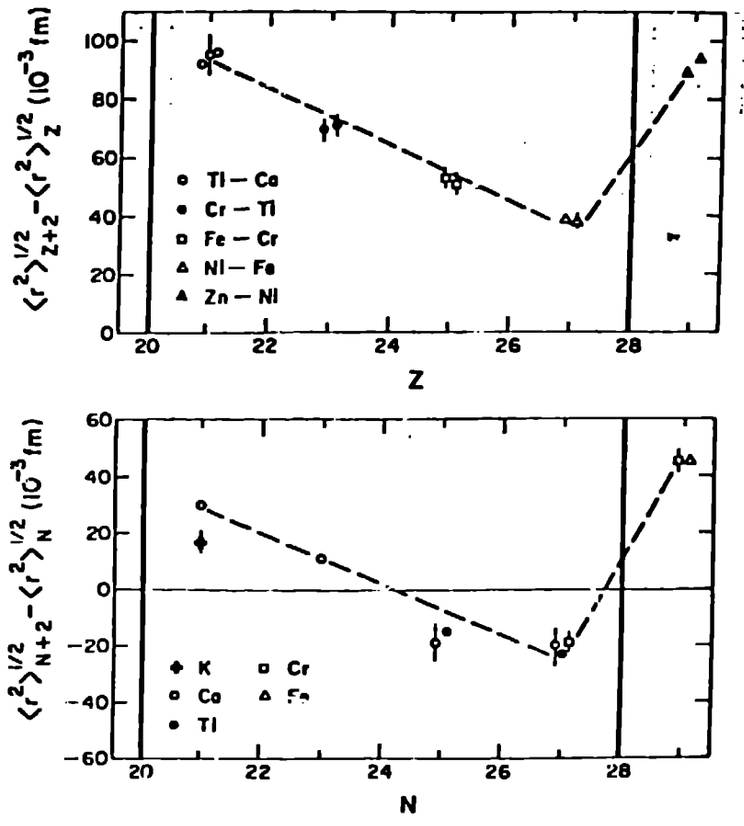

Fig. 7. ΔA=2 isotonic and isotopic rms-charge radii differences.

B. Interpretation and comparison with theory

In the following, I will try to compare the polarization of the charge distribution due to the added protons, which is reflected in the measured isotone shifts, with the polarization of the charge distribution due to the added neutrons, which we observe in the measured isotope shifts directly. The charge distribution densities of two nuclei that differ by two neutrons

(neglecting the neutron form factor) are related by:

$$\rho_{N+2} = \rho_N + \delta\rho_N^{core} \tag{5}$$

Here $\delta\rho_N^{core}$ describes the change of ρ_N due to the interaction with the 2 added neutrons. This change of ρ_N is directly measured as mean-square radius difference $\delta\langle r^2\rangle_N^{core}$. The charge distribution densities of two nuclei that differ by two protons are related by:

$$\rho_{Z+2} = \rho_Z + 2\rho_p + \delta\rho_Z^{core} \quad , \tag{6}$$

where ρ_p is the spatial distribution of the added protons and $\delta\rho_Z^{core}$ describes the polarization of the ρ_Z core due to the added protons. Including the normalization we obtain the change of $\langle r^2\rangle_Z$ that is caused by the interaction with the two added valence protons:

$$\delta\langle r^2\rangle_Z^{core} = \frac{Z+2}{Z}\left[\langle r^2\rangle_{Z+2} - \langle r^2\rangle_Z\right] + \frac{2}{Z}\left[\langle r^2\rangle_Z - \langle r^2\rangle_p\right] . \tag{7}$$

$\delta\langle r^2\rangle_Z^{core}$ can be deduced from the experimentally determined values $\langle r^2\rangle_{Z+2}$ and $\langle r^2\rangle_Z$ by making a model assumption for $\langle r^2\rangle_p$, the spatial distribution of the two added valence protons. We determined $\langle r^2\rangle_p$ by a shell model calculation, using $1f_{7/2}$ harmonic oscillator wave functions for the two added valence protons. The lower shadowed band

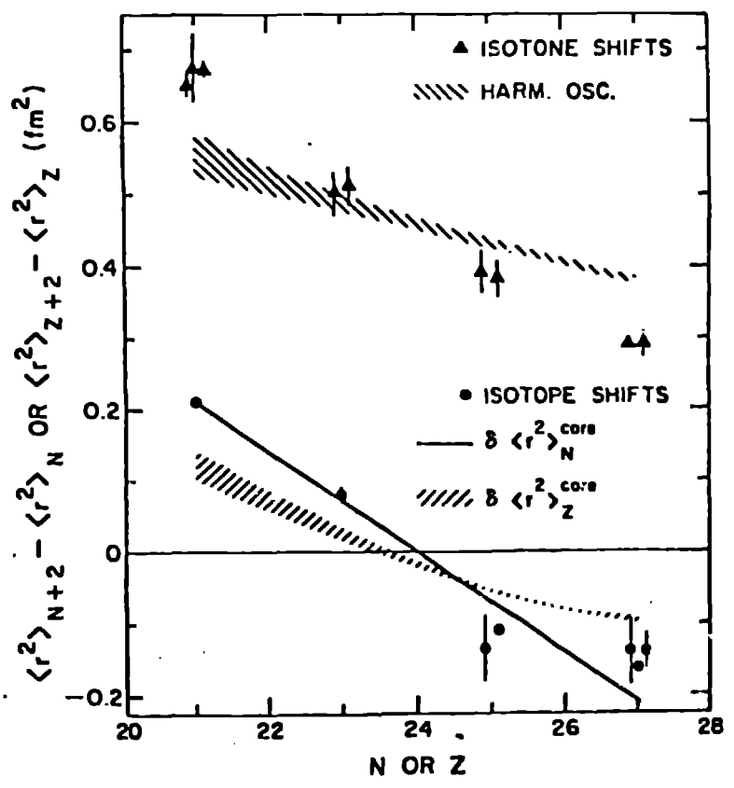

Fig. 8.
Proton core polarization due to protons $\delta\langle r^2\rangle_Z^{core}$ and neutrons $\delta\langle r^2\rangle_N^{core}$.

shows the core polarization due to the added protons $\delta\langle r^2\rangle_Z^{core}$ calculated with formula (7). The upper shadowed curve shows the result of the shell model calculation. The comparison of the shell model calculation and the measured isotone shifts indicates the presence of polarization. $\delta\langle r^2\rangle_Z^{core}$ is positive in the first half of the shell and negative in the second half of the shell, showing the same trend as the directly measured core polarization due to the added neutrons $\delta\langle r^2\rangle_N^{core}$, also displayed in Fig. 8. It is interesting to note that the core polarization due to the added protons, obtained in this way, is about 50% smaller than the core polarization due to added neutrons.

Note that the isotone core polarization effect shows the same feature we observed for isotopes in the Ca nuclei, namely increase of the rms-radii in the first half of the shell and decrease of the rms-radii in the second half of the shell. Again increase and decrease cancel almost totally over the whole shell. Quadrupole deformation parameters β_2 deduced from measured B(E2)-values [13], displayed in Fig. 9, show a systematic behavior that is reminiscent of that observed in the isotope shifts and in the core polarization due to the protons. The deformation for both the isotopes and isotones increases in the first half of the $1f_{7/2}$ shell and decreases in the second half of the $1f_{7/2}$ shell. The increase and decrease cancel almost totally

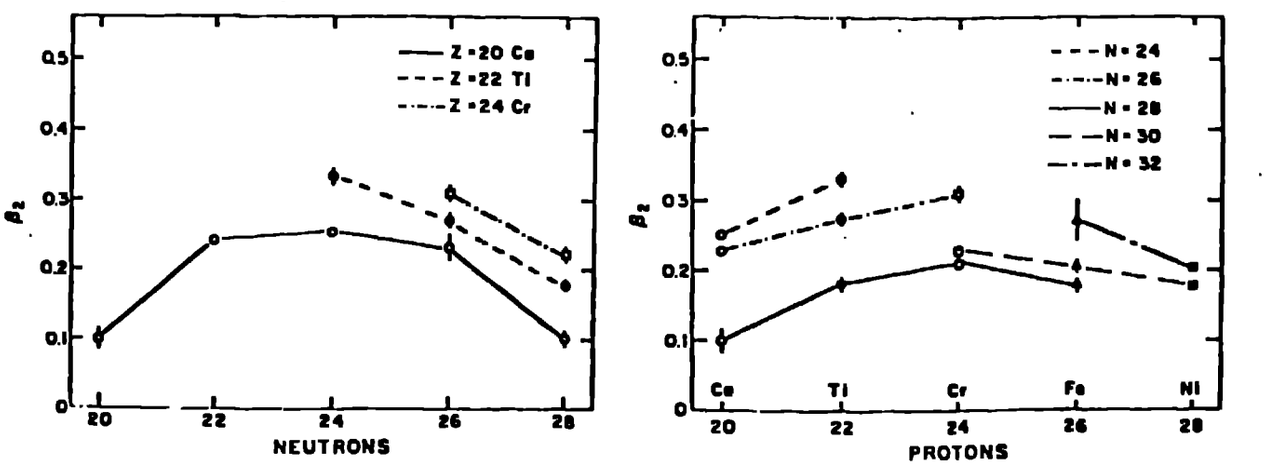

Fig. 9. Quadrupole deformation parameters β_2 for the $1f_{7/2}$ shell nuclei, deduced from measured B(E2)-values.

over the whole shell. The curves for the different elements and isotones are almost parallel. Qualitatively this is in agreement with the observed behavior of the rms-charge radii, suggesting that the observed increase in the rms-radii in the first half of the shell is due to an increase in deformation and the observed decrease in the second half of the shell is caused by a decrease in deformation. At the end of my talk I will come back to this, investigating this point quantitatively.

Fig. 10 displays some of our results for charge distribution differences from our combined analyses of the present muonic data and electron scattering data from Stanford [10]. These figures illustrate the results for the changes in the rms-charge radii differences. The charge distribution difference $^{44}Ca - {}^{40}Ca$ shows that by adding the first four neutrons in the $1f_{7/2}$ shell, the Z=20 proton core is polarized in such a way that charge from the inner part of the nucleus is transferred to the outer part of the nucleus. The opposite effect is observed when the last four neutrons are added into the $1f_{7/2}$ orbital, as can be seen in the examples of $^{48}Ca - {}^{44}Ca$ and $^{50}Ti - {}^{46}Ti$. The charge distribution difference $^{48}Ca - {}^{40}Ca$ illustrates that the observed $\delta\langle r^2\rangle^{1/2} = 0$ is the result of a rather complicated polarization effect. By adding 8 neutrons to ^{40}Ca to form ^{48}Ca, charge from both the inner and the outer part of the Z = 20 proton core is transferred into the surface region of ^{48}Ca.

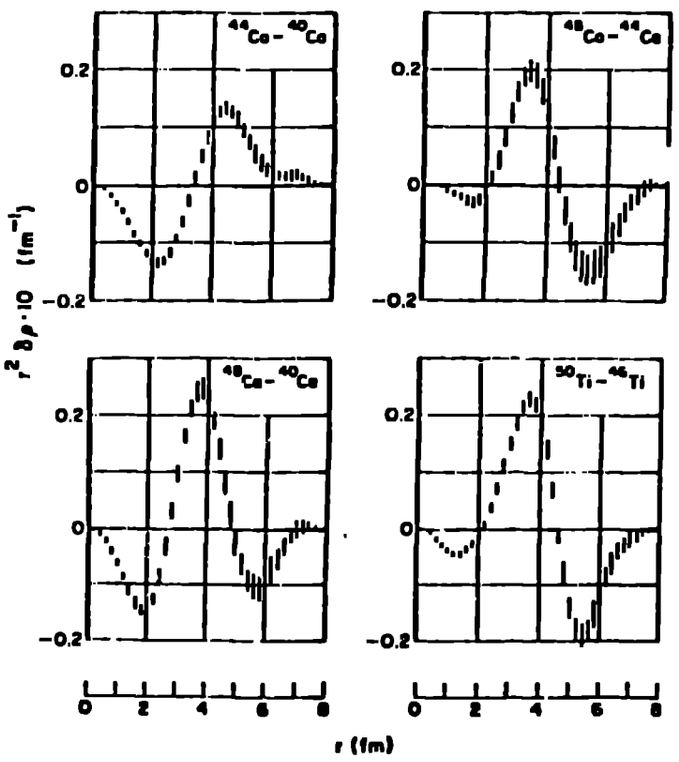

Fig. 10. Charge distribution differences from the combined analyses of the muonic data and (e,e) data.

Fig. 11 shows result of density dependent Hartree-Fock (DDHF) calculations of Negele [14] for the ^{40}Ca charge distribution and for the charge

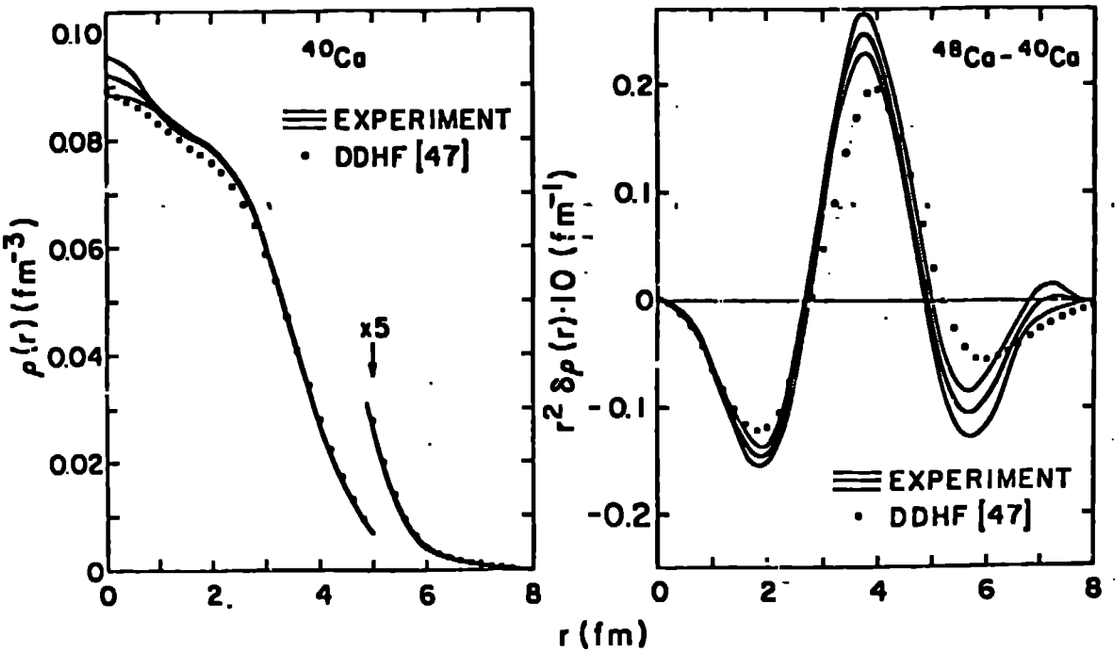

Fig. 11. Comparison of experiment ((e,e) + muonic atom) and theory.

distribution difference ^{48}Ca - ^{40}Ca. Also shown in Fig. 11 are the results of the combined analysis of the present muonic data and electron scattering data. The calculations are in satisfactory agreement with the experiment. The rms-radii and their differences are also in good agreement.

^{40}Ca : $\langle r^2\rangle^{1/2}_{EXP} = 3.481 \pm 0.005$ fm $\qquad \langle r^2\rangle^{1/2}_{TH} = 3.502$ fm

^{48}Ca - ^{40}Ca: $\delta\langle r^2\rangle^{1/2}_{EXP} = (-0.7 \pm 0.9) \times 10^{-3}$ fm $\qquad \delta\langle r^2\rangle^{1/2}_{TH} = 3 \times 10^{-3}$ fm

The success of these calculations in the double closed shell nuclei ^{40}Ca and ^{48}Ca, however, does not necessarily imply that the other $1f_{7/2}$ shell nuclei can be equally well described by DDHF. This is illustrated in Fig. 12, where our $\Delta N=2$ experimental isotope shifts for the Ca nuclei are compared with spherical Hartree-Fock calculations [15]. The calculation does not reproduce the observed almost linear decrease in the shifts for the Ca nuclei. Even Hartree-Fock calculations including nuclear deformation [15] are not in satisfactory agreement with experiment.

Reinhard and Drechsel [15] have shown recently that ground state correlations, neglected in H. F. calculations, are important in isotope shifts. In their calculations the bulk properties of nuclei, varying smoothly and slowly with the nucleon number A, are obtained from spherical Hartree-Fock calculations. In addition they consider not only the influence of static deformations but also the contribution due to zero-point oscillations of the nuclear excitation modes. These contributions come mainly from the isoscalar 2^+ giant resonance, which varies slowly with A, and from the low lying collective 2^+ states, which vary characteristically over the $1f_{7/2}$ shell (see Fig. 9). Both the contribution of the zero point oscillations and the influence of the static deformation are related to experimental B(E2)-values. Including the experimental B(E2)-values [13, see Fig. 9] in their calculations, Reinhard and Drechsel calculated ΔN=2 isotope shifts for the Ca isotopes which are in satisfactory agreement with experiment (see Fig. 12 (H.F+G.S.C.)). This indicates that changes in deformation and zero-point oscillations are important in the Ca isotope shifts. Calculations for other $1f_{7/2}$ shell nuclei have not yet been performed. From the systematics of the β_2 quadrupole deformation parameters shown in Fig. 9, it seems very probable that this kind of calculations, which were very successfull for the Fe, Ni and Zn isotope shifts also, can give satisfactory agreement with experiment for the other $1f_{7/2}$ shell nuclei.

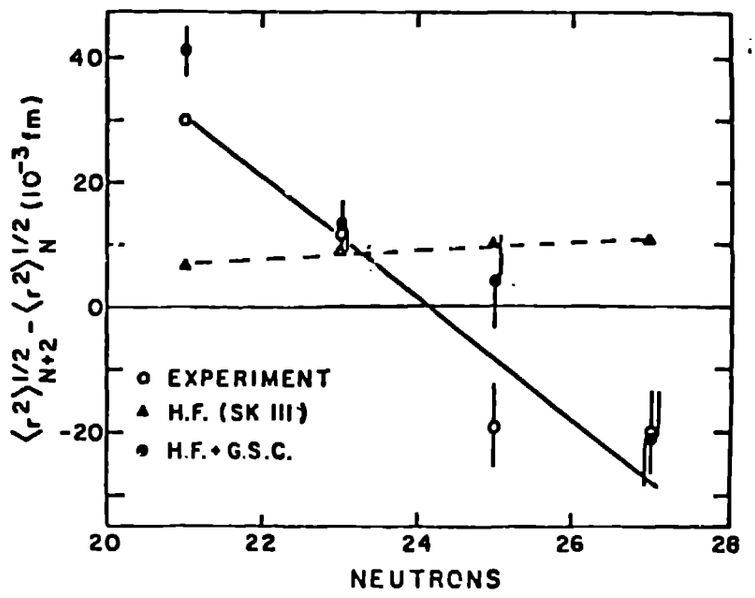

Fig. 12. Experimental and calculated ΔN=2 isotope shifts for the Ca isotopes.

Acknowledgment

The author wishes to thank M. V. Hoehn and E. B. Shera for helpful discussions.

References

1. H. R. Collard, L. R. B. Elton and R. Hofstadter, Nuclear Radii in Landolt-Börnstein I,2, 1 (Springer Verlag Berlin 1967).

2. W. D. Myers, Nucl. Phys. A204, 465 (1973).

3. E. B. Shera, E. T. Ritter, R. B. Perkins, G. A. Rinker, L. K. Wagner, H. D. Wohlfahrt, G. Fricke, and R. M. Steffen, Phys. Rev. C14, 731 (1976).

4. I. Angeli and M. Csatlos, Nucl. Phys. A288, 480 (1977).

5. R. Engfer, H. Schneuwly, J. L. Veuilleumier, H. K. Walter and A. Zehnder, At. Data Nucl. Data Tables 14, 509 (1974).

6. H. D. Wohlfahrt, E. B. Shera, M. V. Hoehn, Y. Yamazaki, G. Fricke, and R. M. Steffen, Phys. Lett. 73B, 131 (1978).

7. H. D. Wohlfahrt, E. B. Shera, M. V. Hoehn, Y. Yamazaki, and R. M. Steffen, to be published.

8. G. A. Rinker and R. M. Steffen, At. Data Nucl. Data Tables 20, 143 (1977).

9. R. C. Barrett, Phys. Lett. 33B, 388 (1970).

10. R. F. Frosch, R. Hofstadter, J. S. McCarthy, G. D. Nöldeke, K. J. Van Oostrum, M. R. Yearian, B. C. Clark, R. Herman, and D. G. Ravenhall, Phys. Rev. 174, 1380 (1968), and J. Heisenberg, R. Hofstadter, J. S. McCarthy, R. Herman, B. C. Clark and D. G. Ravenhall, Phys. Rev. C6, 381 (1972).

11. H. D. Wohlfahrt, O. Schwentker, G. Fricke, H. G. Andresen, and E. B. Shera, to be published.

12. B. Dreher, J. Friedrich, K. Merle, H. Rothhaas, and G. Lührs, Nucl. Phys. A235, 219 (1974).

13. P. H. Stelson and L. Grodzins, Nucl. Data Sheets A1, 21 (1965); A. Christy and O. Hansen, Nucl. Data Tables 11, 281 (1972).

14. J. W. Negele, Invited Talk at the 2nd Nucl. Phys. Div. Conf. of the Eur. Phys. Soc., Crakow (1976); and J. W. Negele, private communication (1978).

15. P. G. Reinhard and D. Drechsel, Z. Phys. A290, 85 (1979).